Electronic Supplementary Information

Large scale oxygen order phase transitions and fast ordering kinetics at moderate temperatures in $Nd_2NiO_{4+\delta}$ electrodes

Sumit Ranjan Maity,[a,b] Monica Ceretti,[c] Ruben De Barros,[c] Lukas Keller,[a] Jürg Schefer,[a] Antonio Cervellino,[d] J. Alberto Rodríguez Velamazan,[e] and Werner Paulus,[c]

[a] Laboratory for Neutron Scattering and Imaging, Paul Scherrer Institut, Villigen CH- 5232, Switzerland

[b] University of Geneva, Department of Quantum Matter Physics (DQMP) 24, Quai Ernest Ansermet CH-1211 Genève 4, Switzerland

[c] ICGM, Université de Montpellier, CNRS, ENSCM, FR-34095 Montpellier, France

[d] Swiss Light Source, Paul Scherrer Institut, Villigen CH-5232, Switzerland

[e] Institut Laue-Langevin, 71 Avenue des Martyrs, F-38042 Grenoble, France

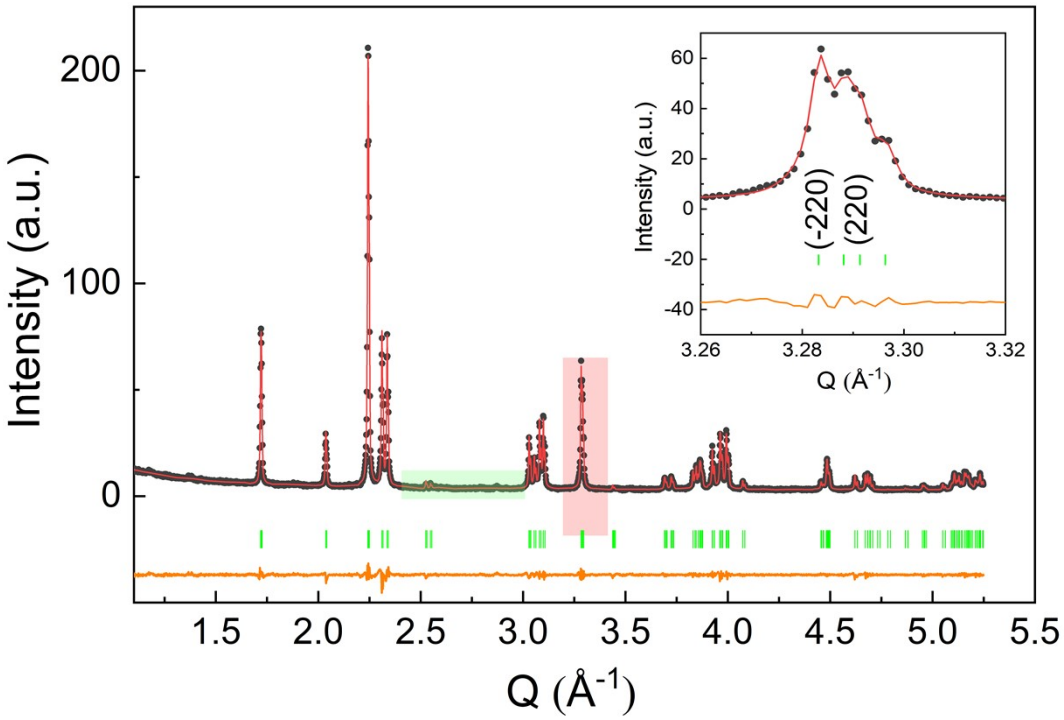

Figure S1: A representative Rietveld fit of the room temperature X-ray powder diffraction data of $Nd_2NiO_{4.23}$ starting phase collected using a Bruker D8 advanced diffractometer using $CuK_{\alpha 1,2}$ radiations (λ_1=1.5405 Å, λ_2 = 1.5443 Å). The circles represent the experimental data while the solid red line displays the calculated pattern. The solid orange line indicates the difference curve. The solid bars in green show the positions of Bragg peaks with monoclinic F112/m space group symmetry. The inset magnifies the region shaded in light orange that demonstrates the monoclinic splitting between (220)/(-220) Bragg peaks at room temperature. The shaded green section shows the absence of oxygen superstructure peaks that are 3 orders of magnitude lesser than the strongest Bragg peaks. Consequently, they are only observed with synchrotron-based measurements and not seen with lab-based X-ray diffraction measurements.

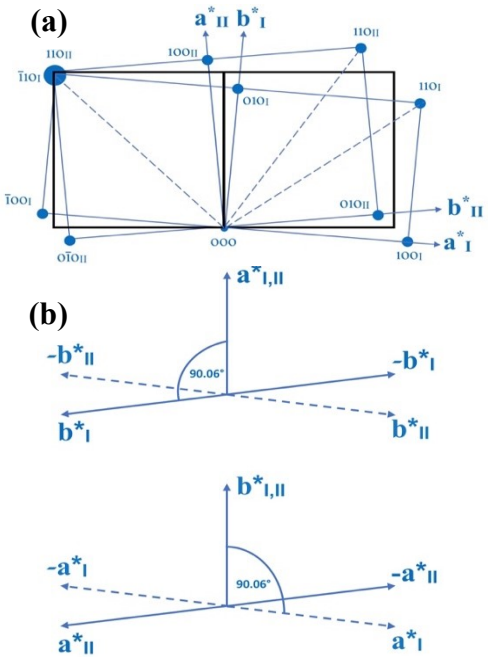

Figure S2: Possible twin domains in $Nd_2NiO_{4.23}$ due to lowering of the structural symmetry from tetragonal F4/mmm. Fig. (a) shows the appearance of two orthorhombic twin domains (in black) due to the loss of 4-fold rotation along the c-axis of the ideal tetragonal (red) unit cell. The loss of mirror planes in the (a-b) plane of the tetragonal phase is then at the origin of the creation of the common plane for the orthorhombic twin domains. Figs. (b) and (c) display possible monoclinic twin domains (in blue), related by [100] and [010], i.e. by rotation around the a* or b*-axis, respectively. In general, an almost perfect overlap between (*hkl*) and $(\bar{h}k\bar{l})$ reflections is achieved in Fig. (b) while it is true for (*hkl*) and $(h\bar{k}\bar{l})$ reflections in Fig. (c) with the c-axis being the monoclinic axis. The loss of mirror planes in the (a-c) and (b-c) plane of the orthorhombic phase is then at the origin of the creation of the common plane for the monoclinic twin domains. This type of twinning is taken as merohedric due to the closeness of the monoclinic angle (γ) to 90°. Such a merohedric superimposition of different reflections, which are not equivalent by symmetry, does not allow in determining their respective structure factors as well as the volume fraction of different twin individuals. This complicates the structure analysis beyond an average tetragonal structural model. The displayed twinning scheme yields a maximum of four monoclinic twin domains for each orthorhombic domain. This results in a total number of 8 monoclinic twin domains due to two orthorhombic domains. The realization of the splitting (due to overlap of twin individuals) of main structural Bragg peaks is a complicated task even with single crystal X-ray diffraction. However, the twining scheme could be realized from the superstructure peaks related to a Bragg peak as a consequence of the twinning that always yields a second orientation of each incommensurate modulations vector, resulting from common (a-c) and (b-c) twin planes and which corresponds in its orientation as being mirrored at these respective planes.

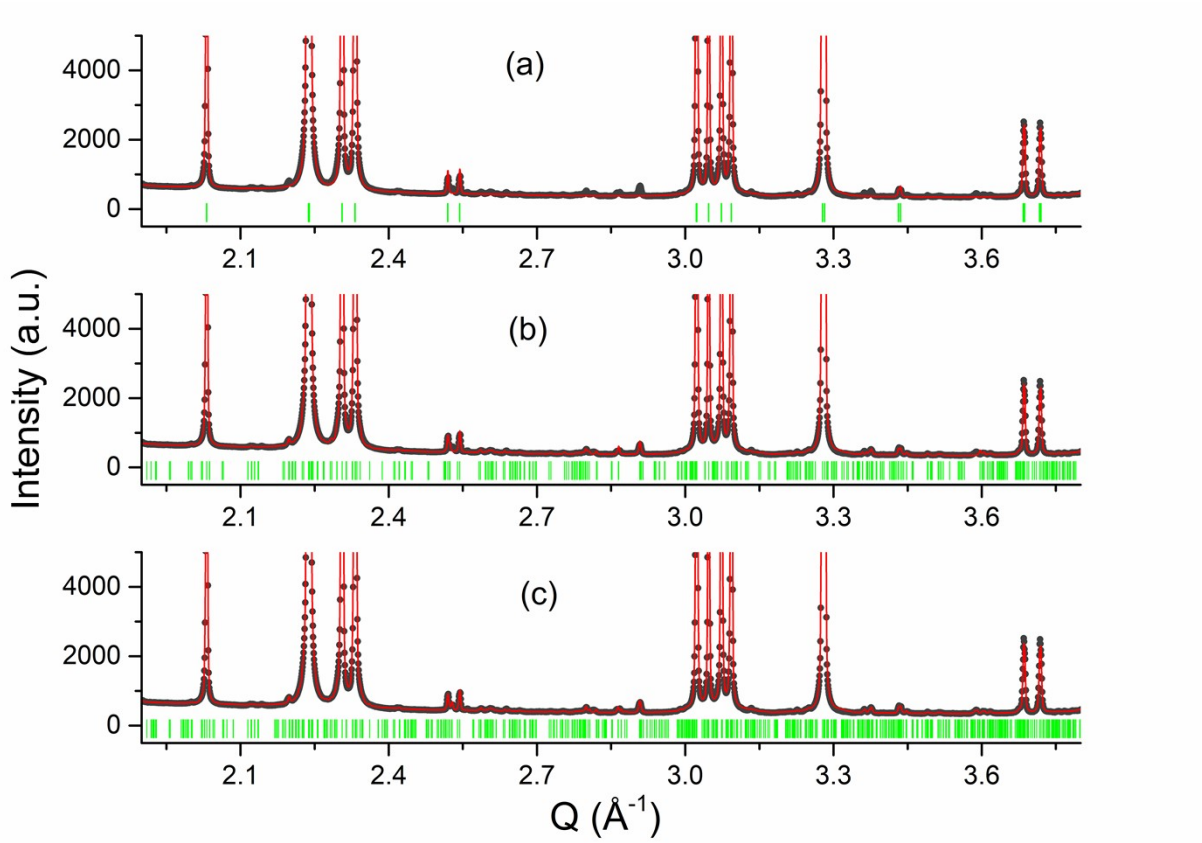

Figure S3: An excerpt of the refined SXRPD data obtained at 373 K during heating. Panel (a) shows the refined pattern without considering the superstructure reflections in the refinement. Panel (b) demonstrates the refined pattern considering only 1st order superstructure reflections while panel (c) depicts the refined pattern considering both 1st and 2nd order satellites. Black circles represent the experimental data while the red solid line denotes the calculated pattern. Solid bars show the positions of Bragg peaks. The modulation vectors are $\mathbf{Q_n}$ = ±0.8245 **a*** ± 0.5230 **b*** at 373 K characterizing phase I in the phase diagram. The measurement was conducted at MS-X04SA in SLS, PSI with λ=0.5646(3) Å.

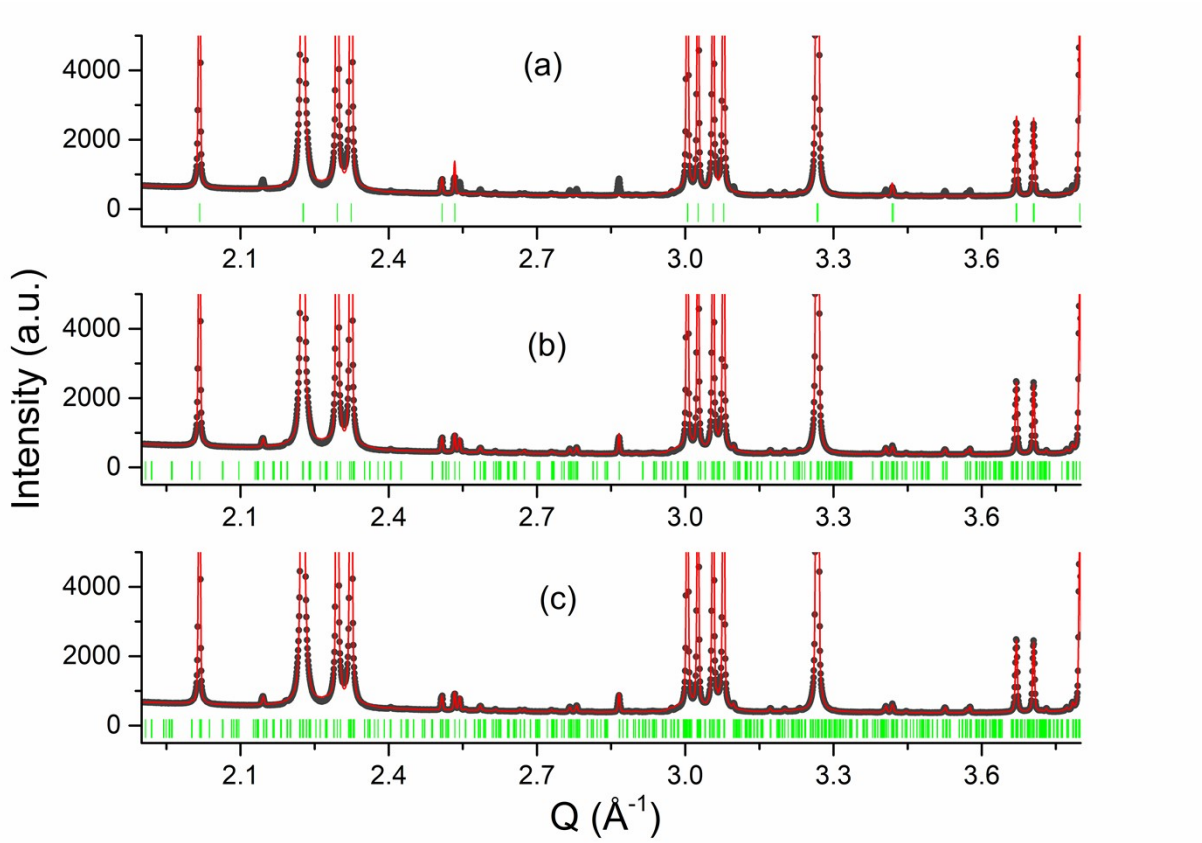

Figure S4: An excerpt of the refined SXRPD data obtained at 703 K during heating. Panel (a) shows the refined pattern without considering the superstructure reflections in the refinement. Panel (b) demonstrates the refined pattern considering only 1st order superstructure reflections while panel (c) depicts the refined pattern considering both 1st and 2nd order satellites. Black circles represent the experimental data while the red solid line denotes the calculated pattern. Solid bars show the positions of Bragg peaks. The modulation vectors are $\mathbf{Q_n}$ = ± 0.7835 **a*** ± 0.5524 **b*** at 703 K characterizing phase V in the phase diagram. The measurement was conducted at MS-X04SA in SLS, PSI with λ=0.5646(3) Å.

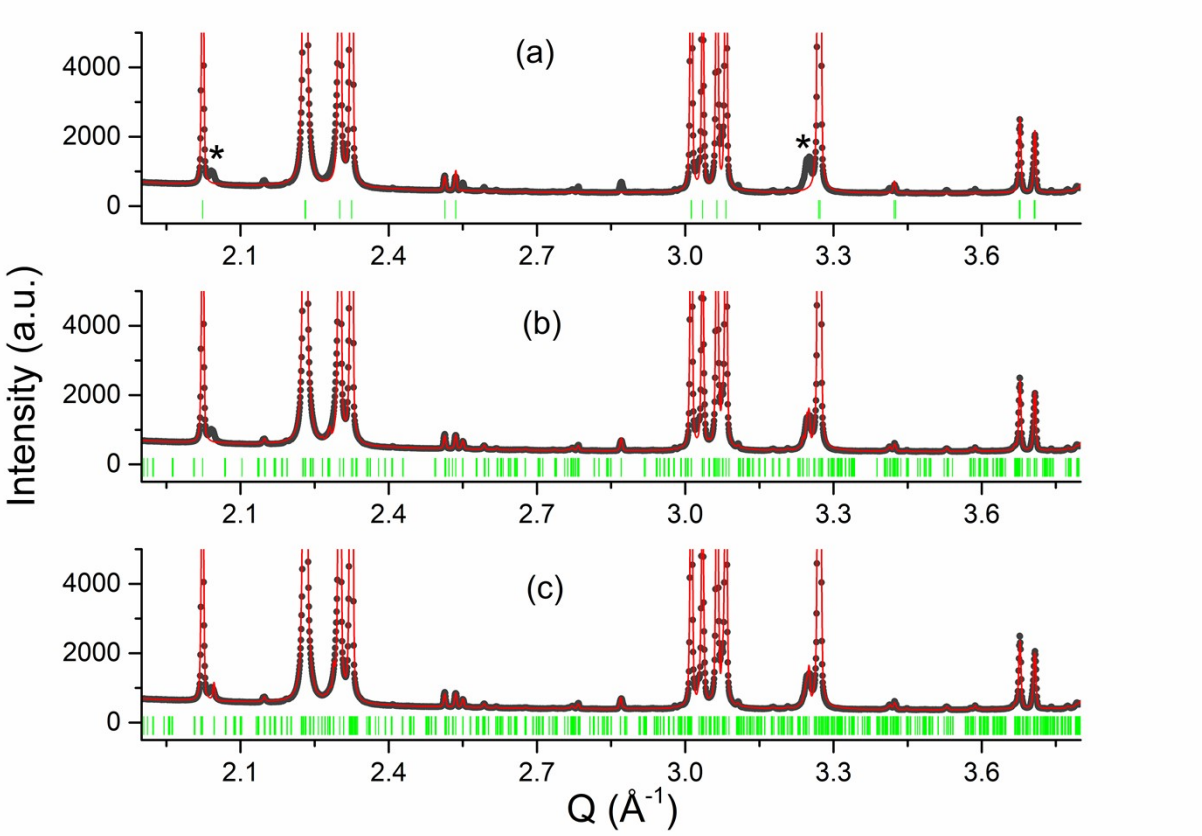

Figure S5: An excerpt of the refined SXRPD data obtained at 583 K during heating. Panel (a) shows the refined pattern without considering the superstructure reflections in the refinement. Panel (b) demonstrates the refined pattern considering only 1st order superstructure reflections while panel (c) depicts the refined pattern considering both 1st and 2nd order satellites. Black circles represent the experimental data while the red solid line denotes the calculated pattern. Solid bars show the positions of Bragg peaks. The modulation vectors are $\mathbf{Q_n}$ = ± 0.7778 **a*** ± 0.5556 **b*** at 583 K characterizing phase III in the phase diagram. The Bragg peaks marked with asterisks are due to the development of a secondary phase as further discussed in the text. The measurement was conducted at MS-X04SA in SLS, PSI with λ=0.5646(3) Å.

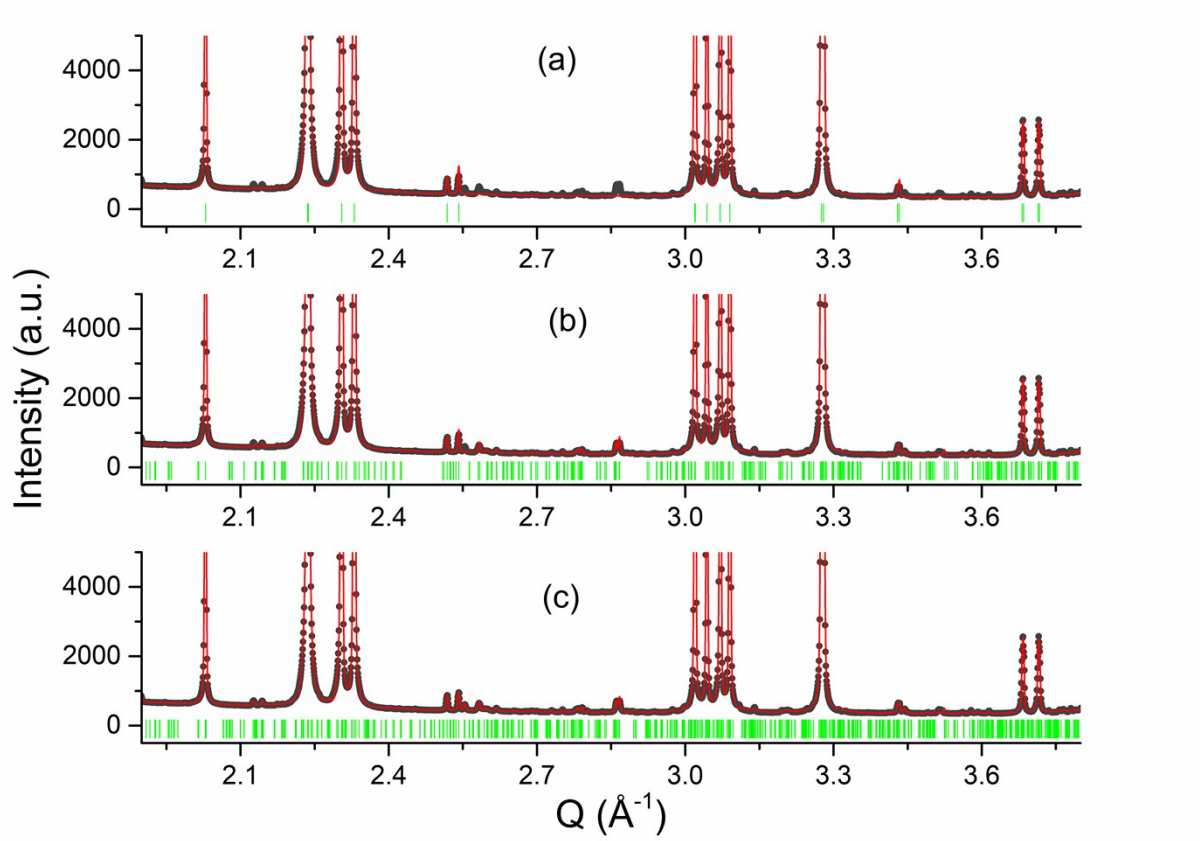

Figure S6: An excerpt of the refined SXRPD data obtained at 433 K during heating. Panel (a) shows the refined pattern without considering the superstructure reflections in the refinement. Panel (b) demonstrates the refined pattern considering only 1st order superstructure reflections while panel (c) depicts the refined pattern considering both 1st and 2nd order satellites. Black circles represent the experimental data while the red solid line denotes the calculated pattern. Solid bars show the positions of Bragg peaks. The modulation vectors are $\mathbf{Q_n}$ = ± 0.7762 **a*** ± 0.5623 **b*** at 433 K characterizing phase II in the phase diagram. The measurement was conducted at MS-X04SA in SLS, PSI with λ=0.5646(3) Å.

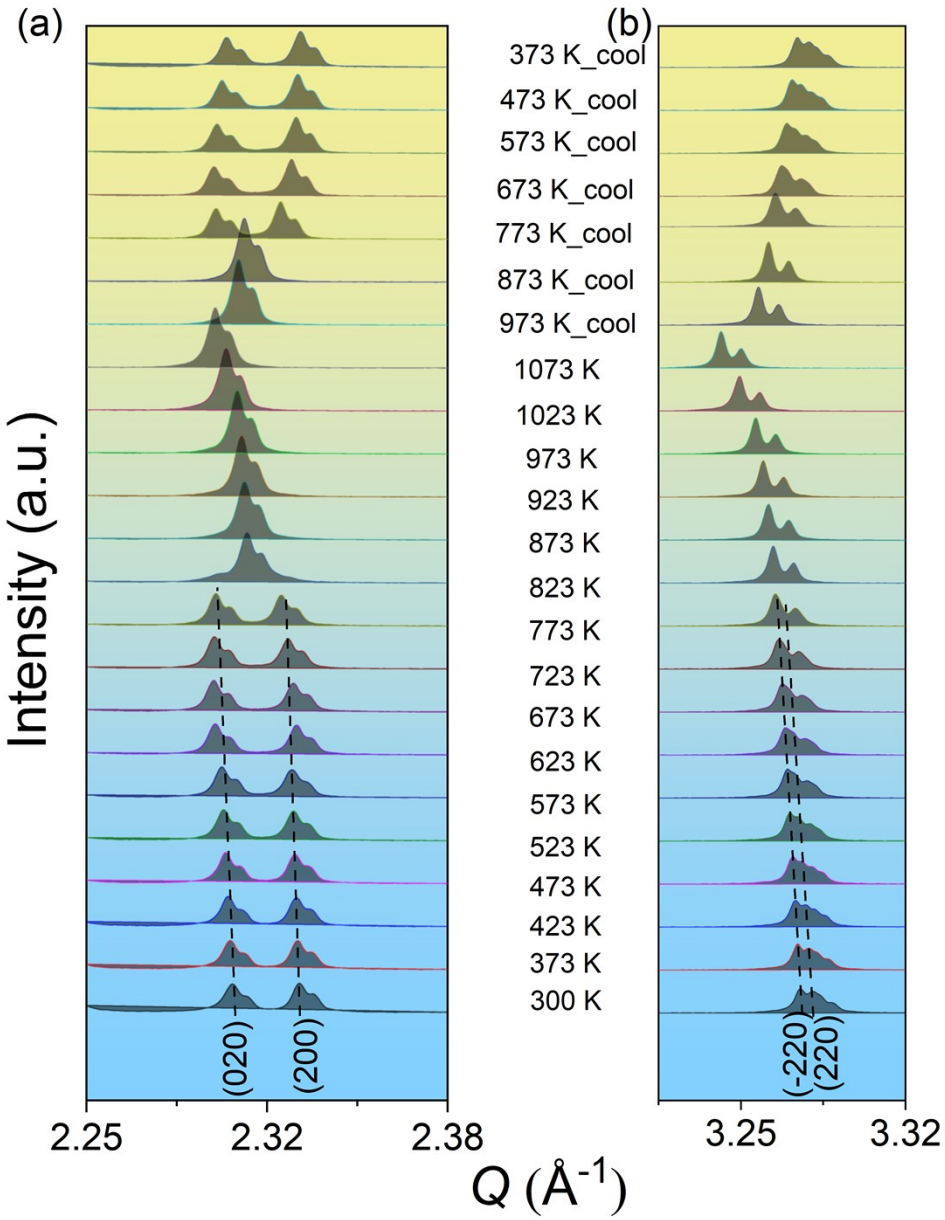

Figure S7: Selected sections of X-ray powder diffraction (XRPD) patterns of $Nd_2NiO_{4.23}$ starting phase collected with a Bruker D8 advanced diffractometer using $CuK_{\alpha 1,2}$ radiations (λ_1=1.5405 Å, λ_2 = 1.5443 Å) equipped with a high-temperature chamber Anton Paar HTK 1200, as a function of temperature in the range of 300-1273 K in air atmosphere. Temperature evolution of (a) (020)/200) and (b) (-220)/(220) structural Bragg peaks during heating from 300 K to 1273 K and cooled back to 300 K. The compound after cooling retains the monoclinic average symmetry as the starting phase though the δ content in the end phase is close to 0.25.

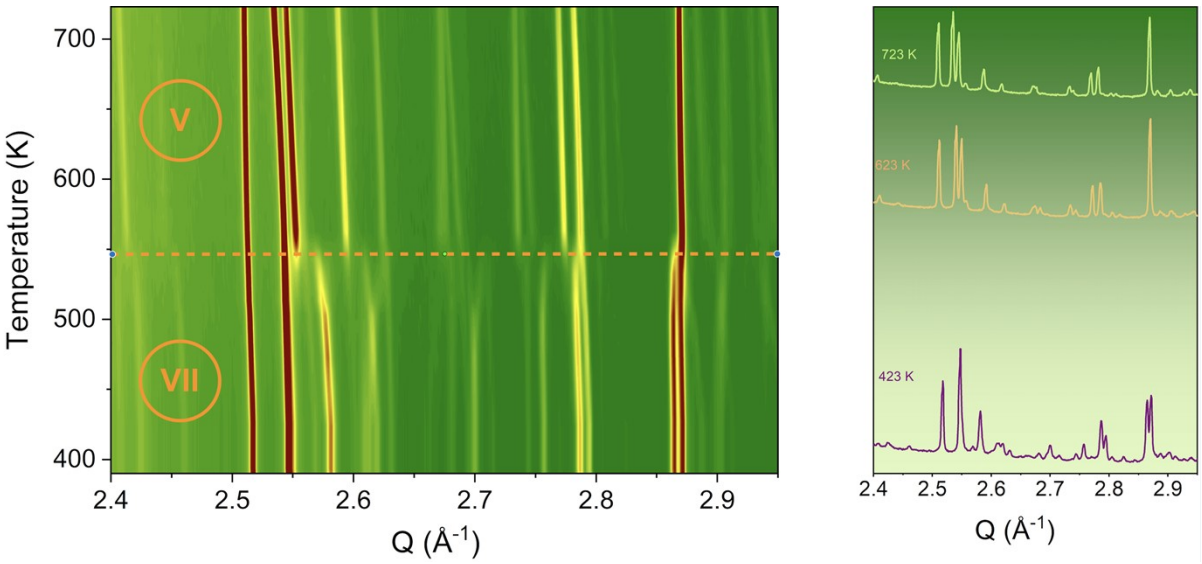

Figure S8: The 2D contour plot representing the thermal evolution of oxygen superstructure reflections during cooling from 873 K in the Q range of 2.4-2.95 Å^{-1}. From the plot, two different phases can be distinguished which are denoted as phase V together with a new phase which shows the same modulation vector as phase II during heating, i.e. $\boldsymbol{Q_n}$ = ± 0.7762 **a*** ± 0.5623 **b*** but which is here denoted as phase VII, as the intensities with phase II significantly change. Illustration of oxygen superstructure reflections at different temperatures in the powder data. The measurement was conducted at MS-X04SA in SLS, PSI with λ=0.5646(3) Å.

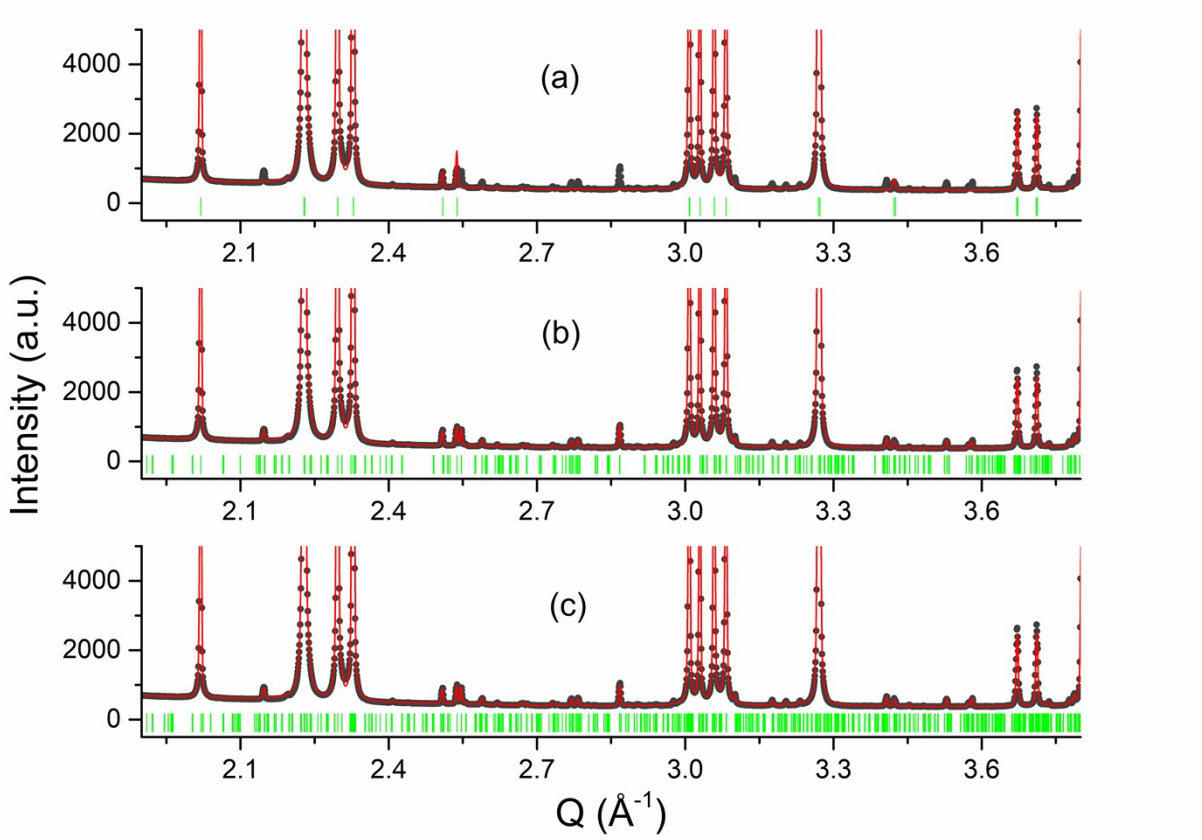

Figure S9: An excerpt of the refined SXRPD data obtained at 623 K during cooling. Panel (a) shows the refined pattern without considering the superstructure reflections in the refinement. Panel (b) demonstrates the refined pattern considering only 1st order superstructure reflections while panel (c) depicts the refined pattern considering both 1st and 2nd order satellites. Black circles represent the experimental data while the red solid line denotes the calculated pattern. Solid bars show the positions of Bragg peaks. The modulation vectors are ± 0.7835a* ± 0.5524b* at 623 K characterizing phase V in the phase diagram. The measurement was conducted at MS-X04SA in SLS, PSI with λ=0.5646(3) Å.

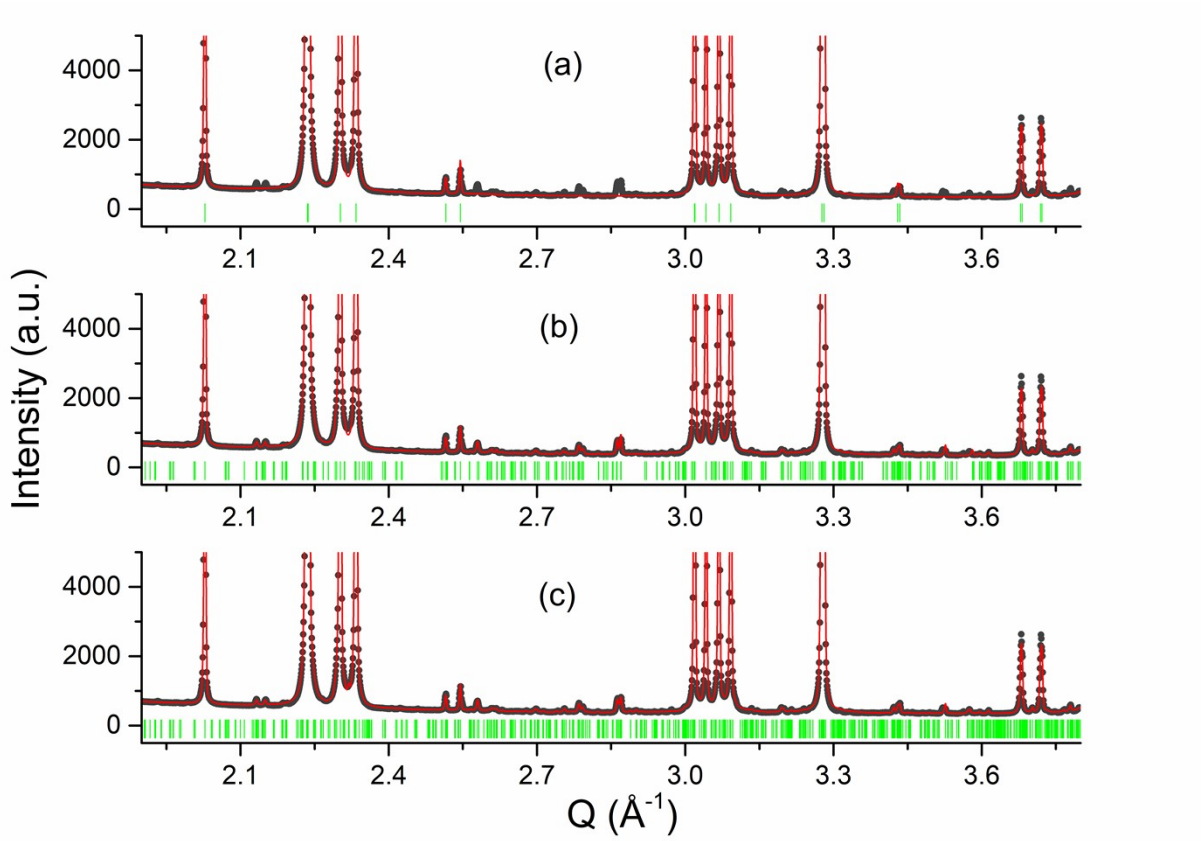

Figure S10: An excerpt of the refined SXRPD data obtained at 423 K during cooling. Panel (a) shows the refined pattern without considering the superstructure reflections in the refinement. Panel (b) demonstrates the refined pattern considering only 1st order superstructure reflections while panel (c) depicts the refined pattern considering both 1st and 2nd order satellites. Black circles represent the experimental data while the red solid line denotes the calculated pattern. Solid bars show the positions of Bragg peaks. The modulation vectors are ± 0.7739a* ± 0.5569b* at 423 K characterizing phase II in the phase diagram. The measurement was conducted at MS-X04SA in SLS, PSI with λ=0.5646(3) Å.